High-order large-eddy simulation of flow over the "Ahmed body" car model

M. Minguez,[1,2] R. Pasquetti,[2] and E. Serre[1]
[1]*Laboratoire M2P2, UMR CNRS 6181, Université Aix-Marseille, IMT La Jetée-Technopôle de Château-Gombert, 38 rue Frédéric Joliot Curie, 13451 Marseille Cedex 20, France*
[2]*Laboratoire J.-A. Dieudonné, UMR CNRS 6621, Université de Nice-Sophia Antipolis, Parc Valrose, 06108 Nice Cedex 02, France*

(Received 21 December 2007; accepted 22 May 2008; published online 2 September 2008)

The structure of the turbulent flow over a simplified automotive model, the Ahmed body (S. R. Ahmed and G. Ramm, SAE Paper No. 8403001, 1984) with a 25° slanted back face, is investigated using high-order large-eddy simulations (LESs) at Reynolds number Re=768 000. The numerical approach is carried out with a multidomain spectral Chebyshev–Fourier solver and the bluff body is modeled with a *pseudopenalization* method. The LES capability is implemented thanks to a spectral vanishing viscosity (SVV) technique, with particular attention to the near wall region. Such a SVV-LES approach is extended for the first time to an industrial three-dimensional turbulent flow over a complex geometry. In order to better understand the interactions between flow separations and the dynamic behavior of the released vortex wake, a detailed analysis of the flow structures is provided. The topology of the flow is well captured showing a partial separation of the boundary layer over the slanted face and the occurrence of two strong contrarotating trailing vortices expanding farther in the wake. The interactions of these large vortices with smaller structures reminiscent of horseshoe vortices, within the shear layer over the slanted face, form large helical structures providing strong unsteady phenomena in the wake. Mean velocity fields and turbulence statistics show a global agreement with the reference experiments of Lienhart *et al.* (DGLR Fach Symposium der AG SRAB, Stuttgart University, 15–17 November 2000). In order to provide a deeper insight into the nature of turbulence, the flow is analyzed using power spectra and the invariant theory of turbulence of Lumley [Adv. Appl. Mech. **18**, 123 (1978)]. © *2008 American Institute of Physics*. [DOI: 10.1063/1.2952595]

I. INTRODUCTION

Aerodynamic features of road vehicles are strongly related to some complex interactions between flow separations and strong trailing vortices expanding far in the wake. Consequently, a detailed knowledge of the physical mechanisms involved in the formation of these flow separations and their interactions with vortical wakes is necessary to successfully design future cars. The Ahmed body,[1] essentially a parallelepiped volume with a slanted face at rear, constitutes the reference car model. Flows over this bluff body reproduce the basic aerodynamic features of cars and simplified shapes favor the comparison between different experimental and numerical studies.

The pioneer experimental work of Ahmed and Ramm[1] pointed out that the flow is essentially controlled, for a given Reynolds number, by the inclination of the slant. At high-Reynolds number, $\mathrm{Re}=U_\infty h/\nu$ (U_∞ is free-stream velocity, h is the height of the body, and ν is kinematic viscosity), the flow is fully unsteady, three-dimensional and shows separations that can be followed by reattachments depending on the slant angle α. Moreover, the flow shows large unsteady phenomena coming from interactions between recirculation bubbles and vortices. All these complex features make computations a challenging task, as illustrated by the ERCOFTAC (Ref. 2) and DFG-CNRS [program large-eddy simulation (LES) of complex flows] benchmarks related to the Ahmed body flow.

In Ref. 1, it is mentioned that $\alpha\approx 30°$ is a critical slant angle for which the topology of the flow is suddenly modified and accompanied by an important decrease of the drag. For subcritical angles, the outer flow may remain attached on the slant, if $\alpha\lesssim 12.5°$, or may partially detach when increasing the incidence up to $\alpha\approx 30°$, then forming a confined recirculation zone. This separation generates a sufficiently strong pressure gradient between the bluff body sides and the slant that brings on the rolling up of the streamlines at the two upper corners of the slant, thus forming two strong contrarotating vortices. These strong vortices are responsible for the high drag (induced drag). This phenomenon is similar to the one occurring on a finite-span wing with a flap of increasing angle of attack. On the contrary, for supercritical angles, the flow totally separates on the slant. This involves a decrease of the previously detailed pressure gradient that inhibits the formation of the strong trailing vortices and consequently induces a decrease of the drag.

For the subcritical and supercritical slant angles $\alpha=25°$ and $\alpha=35°$, respectively, Lienhart *et al.*[3] recently recovered these observations and performed laser Doppler anemometry (LDA) measurements of mean velocity fields and turbulence statistics at Re=768 000. Another experimental study of Spohn and Gillieron[4] at a lower Reynolds number emphasized a more complex topology of the recirculation zone on the slant, which is not closed but contains two separation foci slowly evacuating the fluid above the slant into the wake.

The constant increase of the computer capabilities has

 © 2008 American Institute of Physics

prompted detailed numerical studies of these complex unsteady flows. Numerous attempts to compute the Ahmed body flow by Reynolds averaged Navier–Stokes (RANS) equation approaches have been proposed.[2,5–10] Comparisons with the experiments of Ref. 3 showed that these approaches only succeeded to simulate the flow at the supercritical angle $\alpha=35°$.

The flows computed for the subcritical angle $\alpha=25°$ do not match the experimental results whatever the turbulence models, from the standard $k-\epsilon$ model with wall functions over $k-\omega$ based models (k is the turbulent kinetic energy, ε is the dissipation rate, and ω is the characteristic frequency) and to the explicit algebraic Reynolds stress model and the full Reynolds stress model. Moreover, conclusions of Manceau and Bonnet[2] underlined that whatever the wall function associated with the model, the prediction was not improved.

Generally, this is the partial detachment of the flow on the upper part of the slant that involves the main difficulties. Indeed, the shear due to the recirculation provides small scale structures related to the Kelvin–Helmholtz instability that significantly increases the turbulent stresses, as shown in the LES study of Krajnovic and Davidson.[11] The turbulent kinetic energy measurement of Ref. 3 in the slant mixing layer ($k_{\max}/U_\infty^2 \approx 0.2$) is indeed much higher than in the academical self-similar mixing cases ($k_{\max}/U_\infty^2 \approx 0.035$), for which the models were calibrated. Moreover, the detached eddy simulation (DES) investigation of Menter and Kuntz[9] pointed out a large unsteadiness due to large scale structures related to a spanwise instability.

Consequently, LES may constitute a valuable way to compute the Ahmed body flow, particularly for subcritical slant angles. Indeed, the first LES results[12] captured the topology of the flow and Hinterberger *et al.*[13] showed that the accuracy of the solution is undeniably improved compared to the RANS studies. Particularly, the unsteady phenomena are well described and the solution captures about $\frac{2}{3}$ of the peak of turbulent kinetic energy measured at the beginning of the slant. However, the flow does not reattach over the slant and a quantitative comparison of mean velocities and turbulent stresses profiles shows large differences with experimental data. Small and large scale structures of instability on the slant were reported by DES at Re=768 000 (Ref. 9) and by LES at smaller Reynolds number Re=200 000.[11] However, the statistics of the DES do not compare favorably with the experimental results. More recently, a Lagrangian approach proposed by Fares[14] provided more satisfactory results, but no turbulent stresses profiles were however presented.

There is now a consensus that LES based on subgrid-scale (SGS) models is subject to fundamental limitations in the case of complex flows. Indeed, SGS models have been developed from simple academic flows and so do not contain all the features of a more complex physics. It has been shown for various flows that the shear stress and strain rate tensors involved in SGS models have different topological features. Moreover, Borue and Orzag[15] reported on the basis of numerical simulations of three-dimensional forced homogeneous turbulence, that the energy flux is only weakly correlated with the locally averaged energy dissipation rate, an assumption employed in many eddy-viscosity models.

Alternative LES formulations have been investigated from the 1990s. Some are based on the (unfiltered) Navier–Stokes equations but invoke nonlinear limiters that implicitly act as a filtering mechanism for the small scales [cf. the monotonicity integrated LES approach or more generally implicit LES (ILES) methods[16,17]]. Some others are based on variational multiscale formulations, which essentially introduce stabilization terms in the high frequency range of the spatial approximation[18] (see also Ref. 19). In this case, the Navier–Stokes equations are modified in order to obtain a new set of equations more amenable to approximate the exact solution while preserving the most energetic features of the initial problem. In this spirit, the spectral vanishing viscosity (SVV) technique offers a promising way for high-order LES of complex flows.

In the frame of spectral approximations, which are much less diffusive than low order ones, high-Reynolds number flows are difficult to compute. Indeed the accumulation of energy in the high spatial frequency range generally leads to a divergence of the computations. As a solution, a SVV technique is proposed as an efficient stabilization method of a highly accurate spectral approximation. Contrarily to many stabilization techniques that generally destroy the spectral accuracy of the algorithm, SVV possesses the property of preserving the spectral accuracy. It consists of introducing a viscous term acting only on the highest resolved frequencies. The SVV method was first introduced by Tadmor[20] to solve nonlinear hyperbolic equations, typically the Burgers equation, using standard Fourier spectral methods. Tadmor demonstrated that this artificial dissipation is sufficiently large to stabilize the computations together with preserving the spectral accuracy, even if a postprocessing may be necessary to suppress oscillations when the solution develops shocks. Different works have shown the effectiveness of the SVV method for the LES of incompressible turbulent flows,[21–25] as first suggested by Karamanos and Karniadakis.[21] Our present SVV-LES extends the one described in Ref. 24 for the more academical case of the turbulent wake of a cylinder.

In the present paper, the flow over the Ahmed body with slant angle $\alpha=25°$ (subcritical) at Re=768 000 is investigated. In Sec. II, the physical and mathematical models are presented. The spectral numerical method associated with the SVV approach are briefly described in Sec. III together with the modeling of the bluff body, through a *pseudopenalization* technique. A particular attention is given to the near wall region. We will report some numerical details and information about the LES accuracy in Sec. IV. Detailed analysis of the turbulent flow is provided in Sec. V by showing instantaneous fields and turbulence statistics. Section VI contains some concluding remarks.

II. PHYSICAL AND MATHEMATICAL MODELING

A. Physical problem

The geometry of the car model conforms with the experiments of Ref. 3. The Ahmed body, of length $l=1044$ mm, height $h=288$ mm, and width $w=389$ mm, is placed at $d=50$ mm from the ground, as presented in Fig. 1.

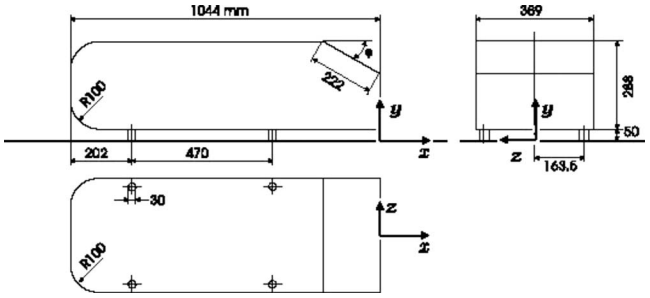

FIG. 1. Sketch with dimensions of the Ahmed body.

The fluid domain is constituted of a tunnel of rectangular section, 1370×1000 mm^2 (in the z-spanwise and y-vertical directions), spreading on four lengths l of the bluff body, which is located at the distance l from the inlet. Consequently, the blockage factor, defined as the ratio between the bluff body section to the channel one, is equal to 8.24% in the computations. This value, which is about two times larger than the value used in the experiments of Ref. 3, 4.24%, allows a reduction of the computational cost. At the inlet, a bulk velocity $U_\infty=40$ m/s is imposed and a stiff variation is used to match the no-slip condition at the ground.

Later on in the text, we mainly use dimensionless values, using h and U_∞ for reference length and velocity, respectively. For the sake of simplicity, we however keep the same notations, knowing that if a dimensioned variable is concerned then we precise its dimension.

B. Mathematical modeling

The flow is governed by the incompressible three-dimensional Navier–Stokes equations for the volume Ω of boundary Γ. In primitive variables and dimensionless form they write

$$\partial_t\mathbf{u}+\mathbf{u}\cdot\nabla\mathbf{u}=-\nabla p+\nu\Delta\mathbf{u}\quad\text{in }\Omega\times\mathbb{R}^+, \tag{1}$$

$$\nabla\cdot\mathbf{u}=0, \tag{2}$$

where t is the time, p is a pressure term, and $\mathbf{u}$ is the velocity of components (u,v,w) in the x-streamwise, y-vertical, and z-spanwise directions, respectively. In dimensionless form, ν is the inverse of the Reynolds number Re. The governing equations must be associated with initial and boundary conditions. At the initial time, the fluid is at rest $\mathbf{u}=\mathbf{0}$. Boundary conditions are only required for the velocity they are of no slip type at the ground $(y=0)$ and around the bluff body, the upper part of the domain $(y=3.47)$ is treated as a free slip surface as, e.g., proposed in Ref. 2, and periodicity is assumed in the spanwise direction. Inlet and outlet boundary conditions are more tricky. At the inlet, the velocity is constant in time and show a stiff variation to vanish at the ground. Turbulent velocity profiles, precomputed from a channel flow simulation at the same Reynolds number, were also tried but did not improve the results, as could be expected from the low average turbulent intensity of 0.25% measured in the experiments.[3] At the outlet $(x=2l)$, convective boundary conditions at the mean flow velocity are applied. In order to avoid any reflection, this must be done with care when spectral methods are concerned since nonlocal approximations are involved. To this end, the following Lagrangian implementation combined with a simple linear interpolation is used:

$$\mathbf{u}^{n+1}(x=2l,y,z)=\mathbf{u}^n(x=2l-U_\infty\Delta t,y,z), \tag{3}$$

where $\mathbf{u}^n$ is the velocity at time t_n and Δt is the time step.

III. NUMERICAL METHOD

A. Spatial approximation

The numerical method is based on a multidomain Chebyshev–Fourier approximation. In the streamwise direction, the computational domain is decomposed in nonoverlapping subdomains of different lengths depending on the flow region. The continuity of the solution at the subdomain interfaces is ensured by using an influence matrix technique, as in Ref. 26. In each subdomain, a collocation Chebyshev method is used in the vertical and streamwise directions, whereas a Fourier Galerkin method is used in the spanwise periodic direction.

The Gauss–Lobatto–Chebyshev (GLC) mesh is especially adapted when boundary layers occur at the boundary of the computational domain, since GLC points accumulate at the end points of the reference interval $(-1,1)$. Thus, the GLC mesh is well adapted to describe the boundary layer that develops at the ground. However, it is also required to take care of the boundary layers that develop around the bluff body. In the streamwise x-direction we make use of the fact that a domain decomposition is implemented by locating subdomain interfaces precisely at the front and rear parts of the Ahmed body (see Fig. 2). Moreover, a subdomain interface also coincides with the beginning of the slant in order to correctly describe the flow at the detachment line. In the vertical y-direction we use a mapping to accumulate grid points at the roof of the car model (see Fig. 2). Such a mapping, $f:(-1,1)\to(0,H)$, where H represents the channel height, is polynomial,

$$y=f(Y,a,b)=\frac{H}{2}[aY+bY^2+(1-a)Y^3]+\frac{H}{2}-\frac{bH}{2},\quad Y\in(-1,1), \tag{4}$$

where (a,b) is a couple of parameters taken equal to $(0.5,0.25)$ in our calculations.

In the z-spanwise direction such strategies are not possible to preserve the possibility of using fast Fourier transform (FFT). However here it is possible to simply refine uniformly the mesh, knowing that the increase of the computational cost with respect to the number of grid points is nearly linear since it is, in fact two-dimensional (2D) like problems that are resolved for each Fourier mode and that the FFT cost is only weakly superlinear.

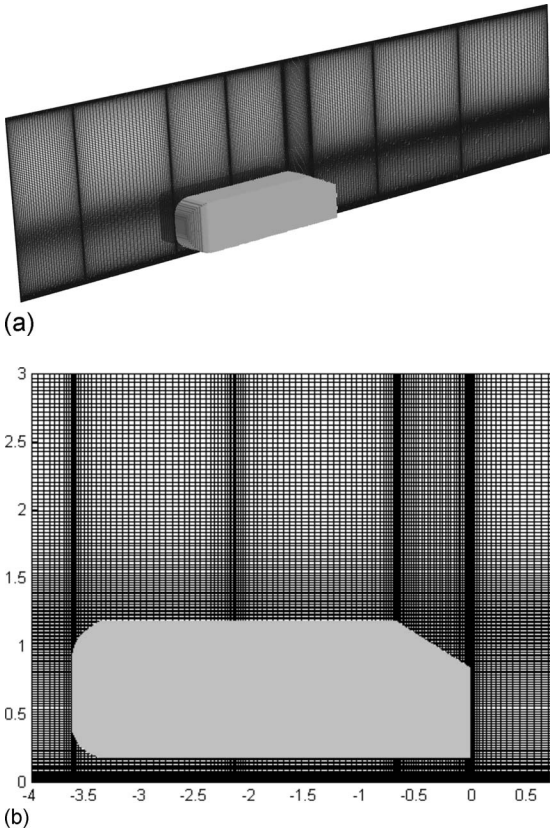

FIG. 2. Visualization of the mesh in the entire channel (a) and around the bluff body (b) in the median vertical plane.

B. Time scheme

The discretization in time is based on a fractional step method. It is globally second order accurate and makes use of the following three steps (see Ref. 27 and references herein for details).

(1) An explicit transport step based on an operator integration factor semi-Lagrangian method and a fourth order Runge–Kutta scheme to handle the nonlinear convective terms.
(2) An implicit diffusion step to handle the linear viscous term. Time derivatives of the velocity components are approximated at the resolution time t_{n+1} with second order backward differences and the pressure is expressed at time t_n, using the so-called Goda scheme, to obtain a provisional velocity.
(3) A projection step to obtain a divergence-free velocity field. It is based on a unique grid "$\mathbb{P}_N-\mathbb{P}_{N-2}$" approximation, i.e., the polynomial degree for the pressure is two degrees less than for the velocity components, so that no boundary conditions are required for the pressure. It is indeed a Darcy-type problem rather than a Poisson one which is solved at this step. In our implementation, the $\mathbb{P}_N-\mathbb{P}_{N-2}$ approximation has been extended to the case of our multidomain approximation: Unknown values of the pressure are considered at all the inner grid points, including the subdomain interface points.

C. SVV-LES approach

As mentioned in the Introduction, the LES capability of the spectral solver makes use of a SVV stabilization technique. In our implementation, the SVV term is introduced in the Navier–Stokes equations through a SVV modified viscous term, so that the numerical approximation, say, $(\mathbf{u}_N, p_{N-2})$, solves (in the collocation Chebyshev–Galerkin Fourier sense) the semidiscrete system,

$$\partial_t \mathbf{u}_N + \mathbf{u}_N \cdot \nabla \mathbf{u}_N = -\nabla p_{N-2} + \nu \Delta_{\mathrm{SVV}} \mathbf{u}_N, \tag{5}$$

$$\nabla \cdot \mathbf{u}_N = 0, \tag{6}$$

where Δ_{SVV} is defined as

$$\Delta_{\mathrm{SVV}} \equiv \nabla \cdot S_N \nabla\,, \tag{7}$$

where S_N is the diagonal operator

$$S_N = \mathrm{diag}\{S^i_{N_i}\}, \quad S^i_{N_i} = 1 + \frac{\varepsilon_{N_i}}{\nu} Q^i_{N_i}, \tag{8}$$

where the subscript i denotes the i-direction (we use here x_i for x, y, and z) where the amplitude coefficient and spectral viscosity operator, ϵ_N and Q_N, appear in one dimension, as introduced in the periodic case (Fourier approximation) in Ref. 20 and in the nonperiodic case (Legendre approximation) in Ref. 28. Let us recall that ϵ_N is usually a $O(1/N)$ coefficient and the operator Q_N acts on the upper part of the Fourier or Chebyshev spectrum of the spectral approximation: With, e.g., φ_k for the Legendre polynomial of degree k, if $v = \Sigma_{k=0}^{\infty} \hat{v}_k \varphi_k$, then $Q_N(v) = \Sigma_{k=0}^{N} \hat{Q}_k \hat{v}_k \varphi_k$, with $1 \geqslant \hat{Q}_k > 0$ if $k > m_N$ and $\hat{Q}_k = 0$ if $k \leqslant m_N$. In practice we use the formula introduced in Ref. 28, $\hat{Q}_k = \exp[-(k-N)^2/(k-m_N)^2]$ if $k > m_N$.

As mentioned earlier, to refine the mesh around the bluff body, a mapping is required. Since the polynomial approximation holds in the reference domain, say, $\hat{\Omega}$, with the mapping $\mathbf{f}: \hat{\Omega} \to \Omega$, the operator S_N is defined as follows:

$$S_N(\nabla \mathbf{u}) \equiv S_N(\hat{\nabla} \hat{\mathbf{u}}) G, \tag{9}$$

where G is the Jacobian matrix of $\mathbf{f}^{-1}$ and $\hat{\mathbf{u}} = \mathbf{u} \circ \mathbf{f}$.

The practical implementation of the operator Δ_{SVV} is based on the introduction of SVV modified differentiation matrices. From the previous definitions of S_N and Δ_{SVV}, we indeed have

$$[\Delta_{\mathrm{SVV}} \mathbf{u}]_i = [\nabla \cdot S_N(\nabla \mathbf{u})]_i = \sum_j \partial_j (\tilde{\partial}_j \mathbf{u}_i), \tag{10}$$

where $\tilde{\partial}_j = (1 + \nu^{-1} \epsilon_{N_j} Q^j_{N_j}) \partial_j$.

D. Obstacle modeling

The Ahmed body is modeled using a volume penalization method. It consists of introducing an additional term canceling (approximately) the velocity field in the volume of the obstacle. The main advantage of such a technique is that

complex geometries may be considered with simple meshes, so that very efficient solvers can be used. Of course the drawback is that locally the approximation is no longer spectral, but this has a limited meaning when the boundary layer cannot be resolved by the mesh. Note that immersed boundary methods, well suited with finite volume methods (see, e.g., Refs. 29 and 30), should be avoided when spectral methods are concerned. Due to the nonlocal feature of spectral approximations, completing the forcing term of the momentum equation with an additional Dirac-like term would induce spurious oscillations which would severely pollute the numerical solution.

Using the standard volume penalization method, Eq. (5) is penalized as follows:

$$\partial_t \mathbf{u}_N + \mathbf{u}_N \cdot \nabla \mathbf{u}_N = -\nabla p_{N-2} + \nu \Delta_{\mathrm{SVV}} \mathbf{u}_N - C\chi(\mathbf{x})\mathbf{u}_N, \quad (11)$$

where C is the penalization constant and $\chi(\mathbf{x})$ is the characteristic function of the obstacle, equal to 1 inside the bluff body and 0 elsewhere.

The penalization term $C\chi(\mathbf{x})\mathbf{u}_N$ must be a few orders of magnitude larger than the other terms of the equations, through the value of the constant C, to finally obtain a $O(1/C)$ residual velocity inside the obstacle.[31] This can provide stability problems if the penalization term is treated explicitly, as it should be in our implementation. To overcome this difficulty, we use the *pseudo penalization* method proposed in Ref. 32. In this method, the penalization term is implicitly introduced through the temporal discretization, with a $O(1/\Delta t)$ penalization coefficient. As detailed in Ref. 32, such an intermediate value is fully justified if the characteristic function of the obstacle is smoothed. Moreover, such a smoothing allows a better approximation of the obstacle and is quite natural in the frame of spectral methods to weaken the expected Gibbs phenomenon. However, as explained now, for the Ahmed body flow it appeared preferable to do not smooth the characteristic function.

E. Near wall treatment

The near wall region around the Ahmed body requires a particular attention, as it is the main location of turbulence production (see, e.g., Refs. 11 and 9). For the past years, many numerical works have focused on this LES-challenging aspect of near wall modeling.[33]

In the literature, all LES investigations of the flow around the Ahmed body use wall functions based on classical log-law (or power laws) profiles to model the viscous sublayer (see, e.g., Ref. 12–14), except in Ref. 11 where a particular topology of grid is used, allowing the resolution of the boundary layer. The global feature of the spectral approximation and of the SVV makes such techniques unusable here.

The thin boundary layer around the Ahmed body being not resolved (see Sec. IV C), a numerical treatment of the solution in this region is required. Such a "near wall treatment" is simply based on numerical tests and reasonable arguments. First, the characteristic function of the obstacle is no longer smoothed. Indeed, the smoothing is here not appropriate because of inducing a thickening of the near wall region and a decrease in the turbulence production. Numerical tests have shown that no Gibbs phenomenon occurred, certainly due to the high frequency dissipation supplied by the SVV term and the $O(h)$ (h, local mesh size) artificial boundary layer induced inside the obstacle by the pseudopenalization technique (see Ref. 32). Second, in order to capture at the best the actual turbulence production in the boundary layer and to keep the global stability of the computation, we have locally relaxed the activation parameter m_N that directly diminishes the range of frequencies where the SVV is active. This is done through a new characteristic function, $\chi_{\mathrm{BL}}(\mathbf{x})$, equal to 1 in the near wall region and to 0 outside. This may be formulated as

$$\partial_t \mathbf{u}_N + \mathbf{u}_N \cdot \nabla \mathbf{u}_N = -\nabla p_{N-2} + \nu \Delta_{\mathrm{SVV}} \mathbf{u}_N - C\chi(\mathbf{x})\mathbf{u}_N + \mathbf{f}_{\mathrm{BL}}, \quad (12)$$

with BL for boundary layer and where

$$\mathbf{f}_{\mathrm{BL}} = \chi_{\mathrm{BL}} \nu (\Delta^{\mathrm{BL}}_{\mathrm{SVV}} \mathbf{u}_N - \Delta_{\mathrm{SVV}} \mathbf{u}_N). \quad (13)$$

The operator $\Delta^{\mathrm{BL}}_{\mathrm{SVV}}$ is defined like Δ_{SVV} but makes use of a greater value of m_N. Note that a smaller value of ϵ_N is also possible to modify the influence of the SVV terms but would be more drastic. Moreover, in order to take into account both the strong anisotropy of the flow in this region and the distribution of grid points in the three directions, the operator $\Delta^{\mathrm{BL}}_{\mathrm{SVV}}$ is anisotropic, which means that values of the parameter m_N differ, depending on the direction. The $\mathbf{f}_{\mathrm{BL}}$ force term is treated explicitly, using a second order Adams–Bashforth extrapolation consistent with the accuracy of the time discretization.

In the following, the SVV technique with near wall correction will be named SVV-NW (SVV-NW approach). Details about the near wall treatment improvements are given in Sec. V D.

IV. COMPUTATIONAL DETAILS

A. Numerical details

The solver is parallelized using the MPI library and optimized on a NEC SX8 parallel-vectorial computer. The computational domain is decomposed in eight subdomains in the x-streamwise direction, each of them being associated with a vectorial processor. Three are localized around the Ahmed body, with one of them on the slant region only (cf. Fig. 2). In each subdomain the space discretization is $41 \times 191 \times 340$, in the x-streamwise, y-vertical, and z-spanwise directions, respectively, so that $N=\{40,190,170\}$, the Chebyshev modes being real whereas the Fourier modes are complex. Consequently, the computations are carried out with a total of about 21×10^6 points. Note that computations have also been carried out with 16 subdomains rather than 8, with roughly the same number of grid points, with very close results.

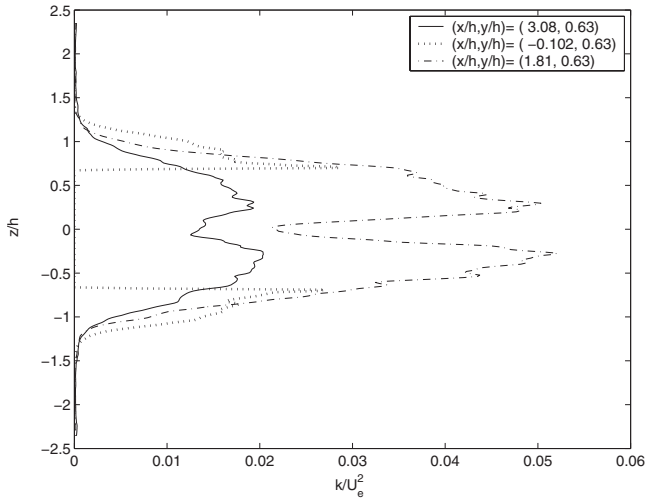

FIG. 3. Turbulent kinetic energy profiles in spanwise direction at three different abscissa.

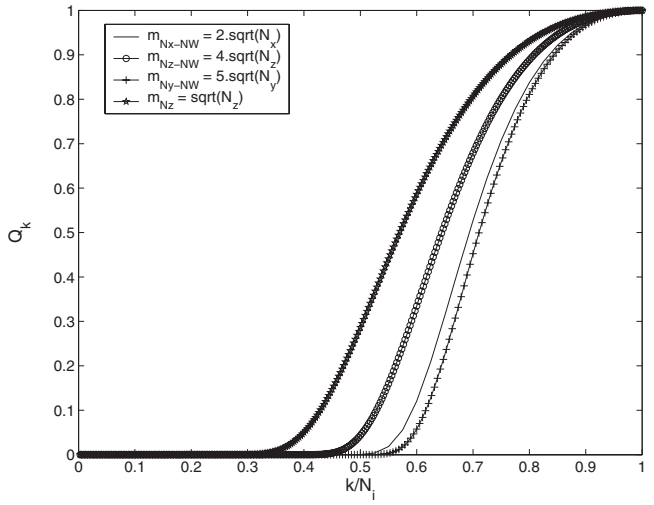

FIG. 4. Spectral kernel of the 1D SVV operator for different values of the threshold frequency m_N, $N=\{40,190,170\}$.

Starting from a flow at rest and by increasing step by step the Reynolds number, a well established turbulent flow has been obtained at Re=768 000 over a dimensionless time $t=100$ using the coarse mesh $N=\{20,85,50\}$. Then, the solution has been interpolated on the fine mesh and computed until $t=160$. The statistics have been converged over the 40 last time units in order to evacuate the residuals of the rough mesh computation. The time unit being equal to h/U_∞, this corresponds to about 0.29 s (physical time). The dimensionless time step was equal to $\Delta t=2\times10^{-3}$ and the CPU time to 9 s for one time step, i.e., approximately 10^{-7} s per iteration and degree of freedom. Globally, the computations have required about 500 CPU h and the fine grid calculations about 18 Gbytes of memory.

In order to verify that the width of the computational domain in the spanwise direction (4.70 h) is large enough to support the hypothesis of periodicity and so to avoid interferences between neighboring Ahmed bodies, Fig. 3 provides z-profiles of the turbulent kinetic energy calculated around the bluff body and farther downstream in the wake. These profiles clearly show that the turbulent kinetic energy vanishes between two neighboring Ahmed bodies, indicating that the implicit alignment of successive bodies has a negligible influence on the turbulence properties.

B. SVV parameters

Each one-dimensional (1D) SVV operator is governed by two parameters, m_N and ε_N, as defined in Sec. III C. Their values must correspond to a compromise between the accuracy of the SVV solution and the stability of the numerical scheme. As expected, see, e.g., the parametric study in Ref. 34 carried out for the wake of a cylinder, the best results were obtained for the largest value of m_N and the smallest value of ϵ_N. Outside the boundary layer, the SVV operator Δ_{SVV} is isotropic with $m_N=\sqrt{N}$ and $\varepsilon_N=1/N$, independently of the spatial (x,y,z) directions. Within the boundary layer, the SVV operator $\Delta_{\mathrm{SVV}}^{\mathrm{BL}}$ is anisotropic with $m_N=\{2\sqrt{N_x},5\sqrt{N_y},4\sqrt{N_z}\}$ and again $\varepsilon_N=1/N$. The corresponding spectral kernels $\hat{Q}_k$ of the SVV operators are shown in Fig. 4 for these three different values of m_N and for $N=\{40,190,170\}$. As it clearly appears, the smaller m_N is, the larger is the range of frequencies on which the SVV acts.

C. Spatial resolution and accuracy

The spatial resolution and accuracy have been checked *a priori* and *a posteriori* both in the near wall and in the near wake flow region. The computational grid such that $N=\{40,190,170\}$ has been sized taking into account both the computational resource and the *a priori* estimation of the characteristic length scales in the boundary layer over the body as well as in the near wake.

Due to the GLC grid and the treatment of the bluff body by a penalization technique, the simulations do not resolve the boundary layers over the Ahmed body. Indeed, in the directions normal to the walls, the wall coordinates (x^+,y^+,z^+) are approximately equal to (80, 400, 400), respectively, see Table I. These values have been obtained from the estimation given in Ref. 14 for the thickness of the viscous boundary sublayer at the end of the vehicle, $\eta_{nw}\approx6.71\,\mathrm{Re}^{-0.9}$, which equals 1 in wall units.

In the near wake region, the grid size is compared with different characteristic length scales usual in homogeneous isotropic turbulence theory.[35] Estimations of the Kolmogorov η and Taylor λ_T length scales are proposed in Ref. 12 for the Ahmed body wake: $\eta\approx1.2\,\mathrm{Re}^{-0.75}$ and $\lambda_T\approx5.5\,\mathrm{Re}^{-0.5}$. The length scale l_0 of the largest anisotropic structures containing energy may be estimated by $l_0\sim\eta\,\mathrm{Re}^{3/4}$. Then the inertial range lies from $l_{EI}\sim l_0/6$, between the anisotropic large ed-

TABLE I. Distances of the first grid points to the car wall: y^+_{top} at the roof, y^+_{bot} at the bottom, x^+_{front} at the front, and x^+_{rear} at the rear of the body.

y^+_{top}	y^+_{bot}	z^+	x^+_{front}	x^+_{rear}
382	460	408	68	82

TABLE II. Characteristic length scales evaluated for the Ahmed body flow at Re=768 000.

	l_0	l_{EI}	λ_T	l_{DI}	η	η_{nw}
In mm	346	58	1.8	0.8	0.013	0.0098
Dimensionless	1.2	2×10^{-1}	6.3×10^{-3}	2.8×10^{-3}	4.63×10^{-5}	3.4×10^{-5}

dies and the isotropic small eddies, to $l_{DI}\sim 60\eta$, between the inertial and dissipative range. All these length scales are given in Table II.

Thanks to the positioning of the subdomain interfaces and to the mapping in the vertical direction, the resolution in the near wake region (i.e., spatial spacing Δx, Δy, and Δz) is in the range $[0.44\lambda_T;11.29\lambda_T]$, $[0.057\lambda_T;5.19\lambda_T]$ for the (x,y) Chebyshev directions, respectively, and $\Delta z=2\lambda_T$ for the homogeneous Fourier direction. Consequently, the grid size allows the resolution of structures within the inertial range.

The numerical resolution has been checked *a posteriori* both in the near wall region and in the wake. Over the body, the wall coordinates may be estimated using the friction velocity u_τ calculated from the mean flow boundary layer equation (see, e.g., Refs. 35 and 36),

$$\langle -u'v'\rangle + \nu\partial_y\langle u\rangle \approx \langle -u'v'\rangle = u_\tau^2, \tag{14}$$

where $\langle u\rangle$ is the mean value of the streamwise velocity and u' and v' are the fluctuations in x- and y-directions, respectively. Note however that if one restarts from the SVV stabilized Navier–Stokes equations, then one obtains from the balance of the mean forces,

$$\langle -u'v'\rangle + \nu\tilde{\partial}_y\langle u\rangle = u_\tau^2, \tag{15}$$

through the SVV stabilized operator $\tilde{\partial}_y$ defined in Sec. III C, the contribution of some "subgrid forces" appears now. Once knowing u_τ one can compute the distance of the first grid points to the wall, say, h, in wall units, hu_τ/ν.

Values obtained from the Eqs. (14) and (15) have been computed over the roof and at the ground downstream in the wake (see Fig. 5). One observes that when using Eq. (14), the viscous term may indeed be neglected whereas when the SVV stabilization is included, the result is slightly different, especially at the ground. In any cases, over the roof, the resolution is about $y^+\approx 350$, which confirms the *a priori* estimation given previously. Over the ground, the value of y^+, close to 4, indicates a much better resolution with a first grid point in the viscous sublayer. This results from the accumulation of the GLC grid points close to the ground.

The numerical resolution has been checked by analyzing Fourier and Chebyshev 1D spectra of the velocity component fluctuations at different locations (see Fig. 6). Spectra decays of more than two orders of magnitude indicate a satisfactory numerical resolution. Similar decays are also found in the wake. As expected we notice that all the spectra show that the dissipation is essentially active from the threshold frequency m_N of the SVV stabilization. Note that satisfactory spectral decays only indicate a satisfactory resolution of the equations that are solved numerically, i.e., the SVV stabilized the Navier–Stokes equations together with the NW treatment, but of course do not provide a validation of this modeling.

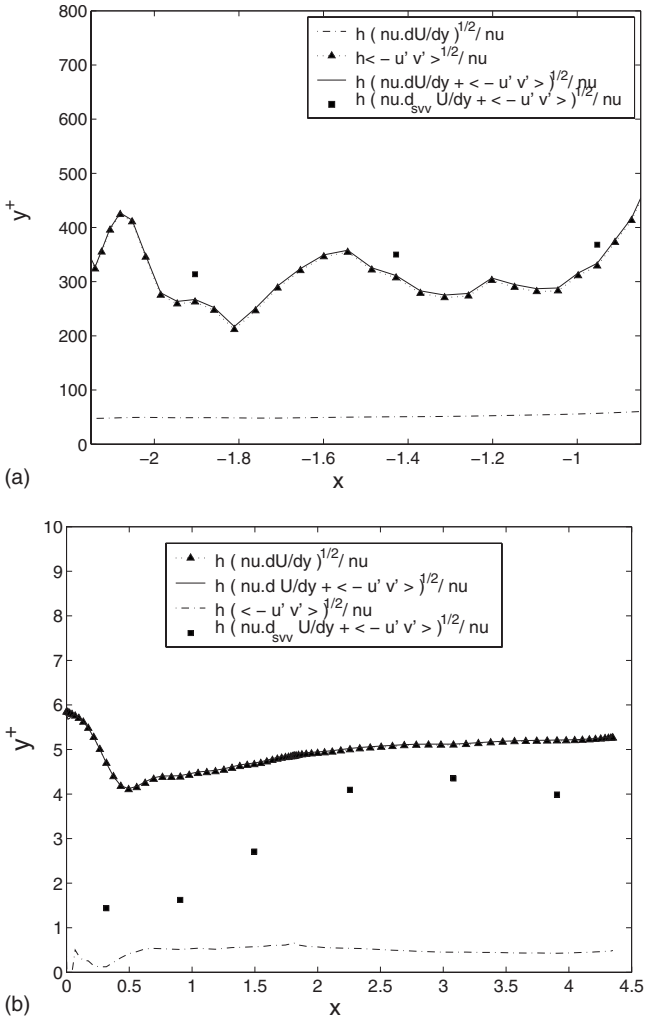

FIG. 5. Resolution on the roof (a) and downstream at the ground (b): y^+ in the streamwise direction and in the symmetry plane. Here d_{SVV} corresponds to $\tilde{\partial}_y$ and $U=\langle u\rangle$. Contributions of the different terms of simplified equations of boundary layer (14) and (15).

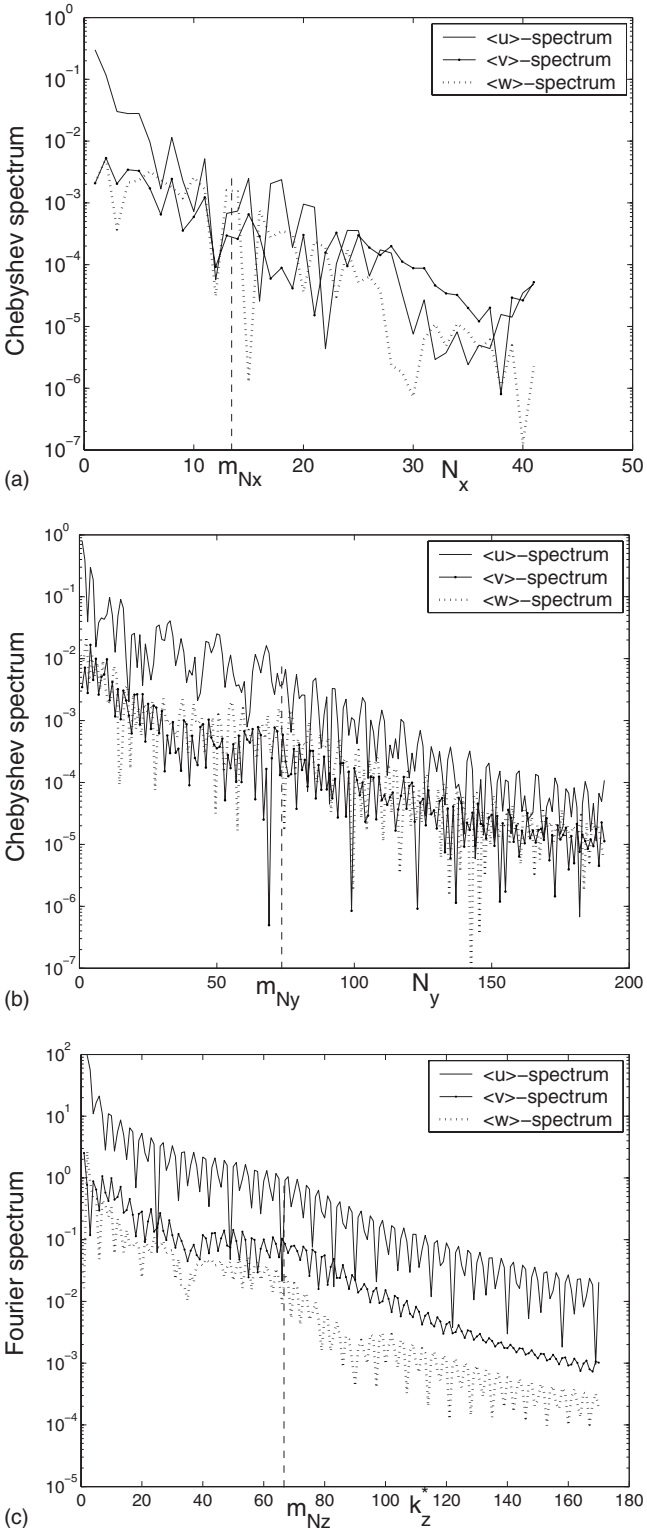

FIG. 6. Spectrum of the mean velocity components in the boundary layers around the bluff body: (a) x-Chebyshev spectra on the roof at ($y=1.18$, $z=0$), (b) y-Chebyshev spectra on the lateral wall at ($x=-0.91$, $z=0.69$), and (c) z-Fourier spectra on the roof at ($x=-0.91$, $y=1.18$).

V. RESULTS

Instantaneous quantities as well as turbulence statistics are presented in this section. The simulations show complex time-dependent and three-dimensional flow features around the bluff body in global agreement with the LDA measurements of Lienhart *et al.*[3]

A. Instantaneous and mean flow fields, flow structures

The flow appears highly turbulent, particularly over the slant, which was not mentioned in the pioneer study.[1] This is, e.g., pointed out by the Fourier analysis of the time variations of the streamwise velocity at different points (see Fig. 7).

The topology of the flow is firstly described by showing the mean 2D streamlines in the plane $z=0$ (Fig. 8). The flow separates and then reattaches both on the leading edge of the body front at $x=-3.3$ and at the sharp edge between the roof of the body and the slant surface. In the front part similar recirculation regions also develop on the lateral sides.

The separation at the body front is characterized by a thin bubble with mean length of 0.7 in the streamwise direction that induces an unsteady recirculation region. The bubble pulsates at a Strouhal number (dimensionless frequency) equal to 0.15 [Fig. 7(a)], whereas the transverse vortices, related to the Kelvin–Helmholtz-like instability within the separated shear layer over the recirculation, travel at a Strouhal number one order of magnitude larger [Fig. 7(b)], as previously observed in the experiments of Ref. 4.

On the roof, the flow reattaches at $x=-2.6$ (see Fig. 8). The turbulent boundary layer that which develops behind the bubble thickens in the streamwise direction to finally reach a dimensionless thickness of $\delta=7.5\times10^{-2}$.

Actually, the occurrence at Re=768 000 of this thin bubble on the front part of the body remains an open question. In the present computations, we can reasonably admit that it could be involved by two main effects. First, the confinement effect imposed by the top boundary condition and the periodicity in the spanwise direction might increase the flow acceleration in the foremost part of the body and the subsequent adverse pressure gradient on the beginning of the roof, possibly up to separation. Second, a too weak level of turbulence in this flow region (compared to an actual flow in experiments) might support the detachment, as the turbulence tends to attach the flow. That certainly results from a too large dissipation by the SVV related to a too coarse grid in the NW region, despite using a NW treatment (see Sec. III E). Nevertheless, we should also underline that most of the studies (including the experiments of Ref. 3) only focus on the slant part and on the near wake of the bluff body and consequently do not provide any available data for the upstream flow. Moreover, some experimental[4] and numerical[11] studies at lower Reynolds number (Re=8322 and Re=2×10^5, respectively) and at higher Reynolds number[37] (Re=1.17×10^6) have recovered these recirculations on the front part of the body. Consequently, it is not clear right now if their presence is actual or an artifact of the numerical modeling.

The flow again separates at the beginning of the slant surface and then tends in the mean to reattach on the slant back as observed in the experiments of Ref. 3. This is clearly shown by the three-dimensional computed streamlines in Fig. 9(a). Nevertheless, contrary to the experiments, the recirculation zone has a nonconstant thickness in the spanwise direction with a weaker intensity and smaller size around the

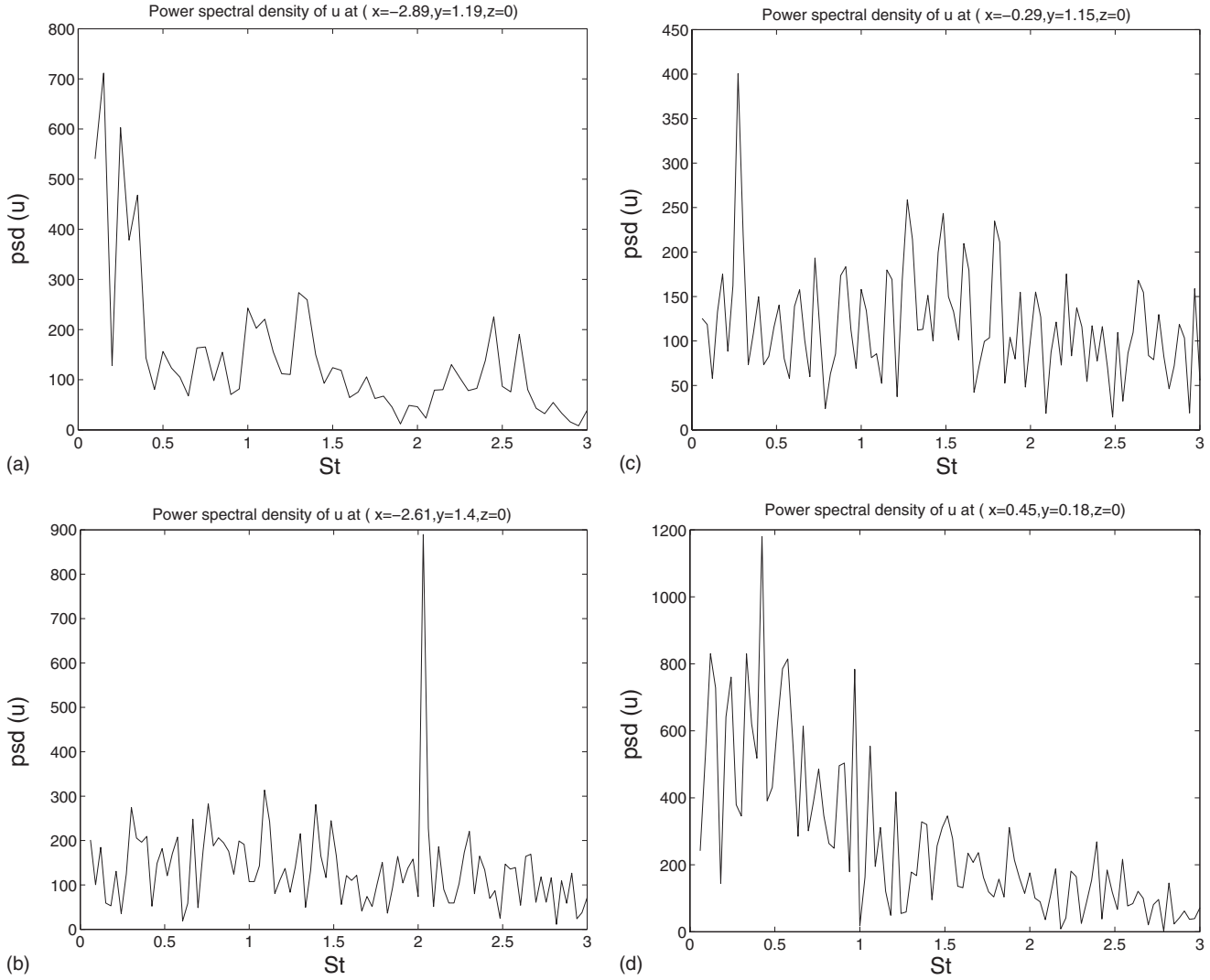

FIG. 7. Power spectral density of the time variations of u at different points over the bluff body; see points A, B, C and D of Fig. 8.

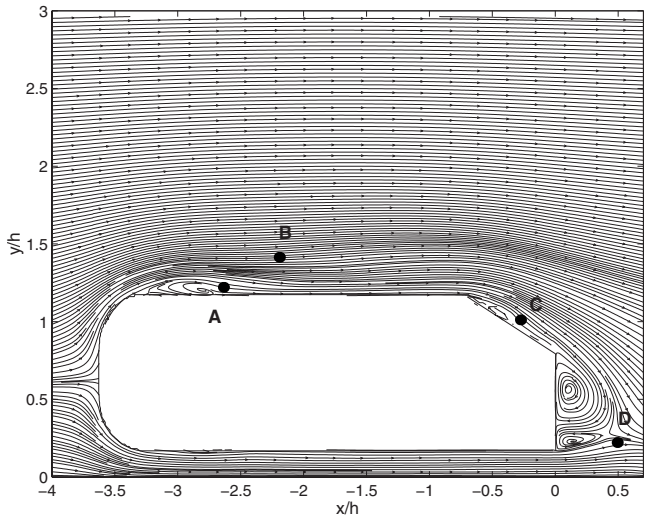

FIG. 8. 2D streamlines computed from the mean 2D velocity field ($\langle u \rangle$, $\langle v \rangle$) in the plane $z=0$ and locations of the temporal measurement points.

symmetry plane $z=0$. Actually, the flow recirculation appears divided in two bubbles, symmetrically located around the symmetry plane. This is supported by the isosurface of the dimensionless turbulent kinetic energy k (reference value U_∞^2) [Fig. 9(b)], which shows a large production of turbulent kinetic energy at the beginning of the slant with two confined regions where the turbulent kinetic energy is maximum. A similar feature is mentioned in the experiment of Ref. 4 at Reynolds number Re=8322.

At the same time, the flow separates at the two edges between the slant and the lateral surfaces of the body. This results in two large counter-rotating conelike trailing vortices that spread farther in the wake [Fig. 9(a)]. These longitudinal vortices correspond to the lowest pressure regions in the flow as it is illustrated in Fig. 9(c) by the isosurface of the mean pressure. Qualitatively, they are similar to those measured in the near wake,[3] as shown by comparing the velocity vector fields (see Fig. 11). A more quantitative comparison is also proposed in Fig. 11 by comparing isocontours of the streamwise velocity. In the near wake the size and the location of the trailing vortices are close to the experimental measurements. Farther in the wake ($x=1.74$), the agreement remains

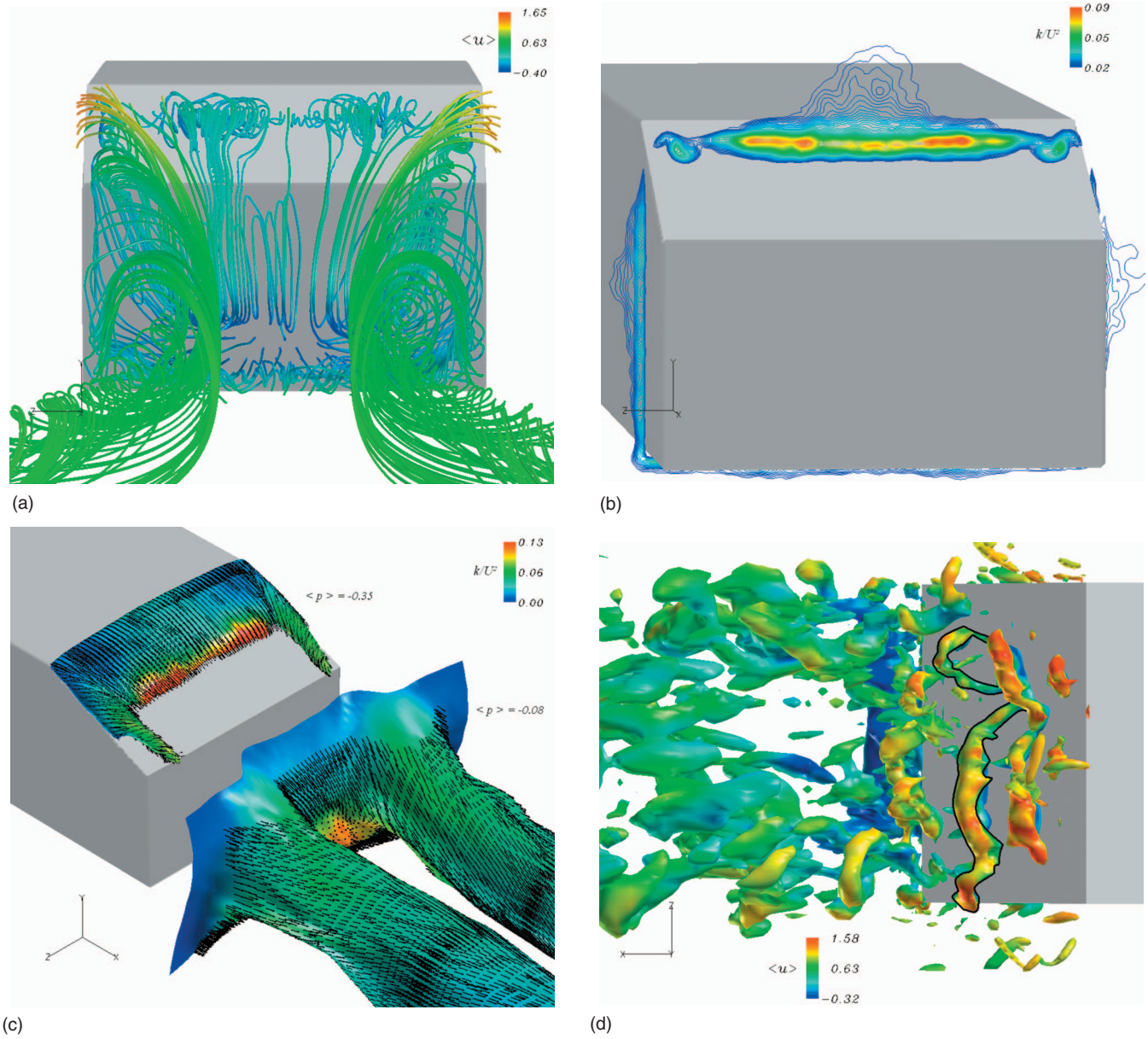

FIG. 9. (Color) Visualization of the vortical structures in the wake of the Ahmed body (Re=768 000): (a) Mean three-dimensional streamlines in the wake colored by the mean streamwise velocity $\langle u \rangle$; (b) isocontour of the turbulent kinetic energy k on the slant; (c) isosurfaces $\langle p \rangle = 0.25$ and $\langle p \rangle = -0.07$ of the mean pressure, colored by the dimensionless turbulent kinetic energy k and showing the velocity field on the slant and in the wake; and (d) isosurface of the pressure fluctuations colored by the mean streamwise velocity $\langle u \rangle$ on the slant and in the wake. Contours of structures reminiscent of horseshoe vortices are blackened.

reasonable even if the vortex core is slightly larger and the vortex center is located slightly lower ($y \approx 0.45$) than in the experiments ($y \approx 0.5$). In the yz-plane $x=1.74$, within the vortex cores, the difference between the minima of streamwise velocity is less than 8%.

These trailing vortices can interact with vortical structures forming over the slant. Indeed, the Kelvin–Helmholtz instability that develops at the shear layer between the slant recirculation and the above free-stream velocity generates vortices parallel to the separation line, which are convected downstream. Then, due to the z-spanwise inhomogeneity of the slant recirculation previously described, these structures are slightly lifted within the shear layer at about halfway down the slant. Their shape is reminiscent of those of the classical horseshoe vortices as shown by an instantaneous isosurface of the pressure fluctuations in Fig. 9(d). Such structures are not observed in RANS studies but have been already reported in the LES (Ref. 11) and confirmed in the DES.[9] The interaction of the large trailing vortices with the smaller horseshoe vortices provides helical structures that roll up around the trailing vortices in the wake of the body [Fig. 9(d)]. As a consequence, the temporal spectrum [Fig. 7(c)] reveals a multifrequency regime with however a dominant Strouhal number of 0.27 related to the horseshoe vortices.

Behind the slant, the flow recirculates along the back of the bluff body (see Figs. 8 and 10) with a dominant Strouhal number equal to 0.42 [Fig. 7(d)]. The flow recirculation is

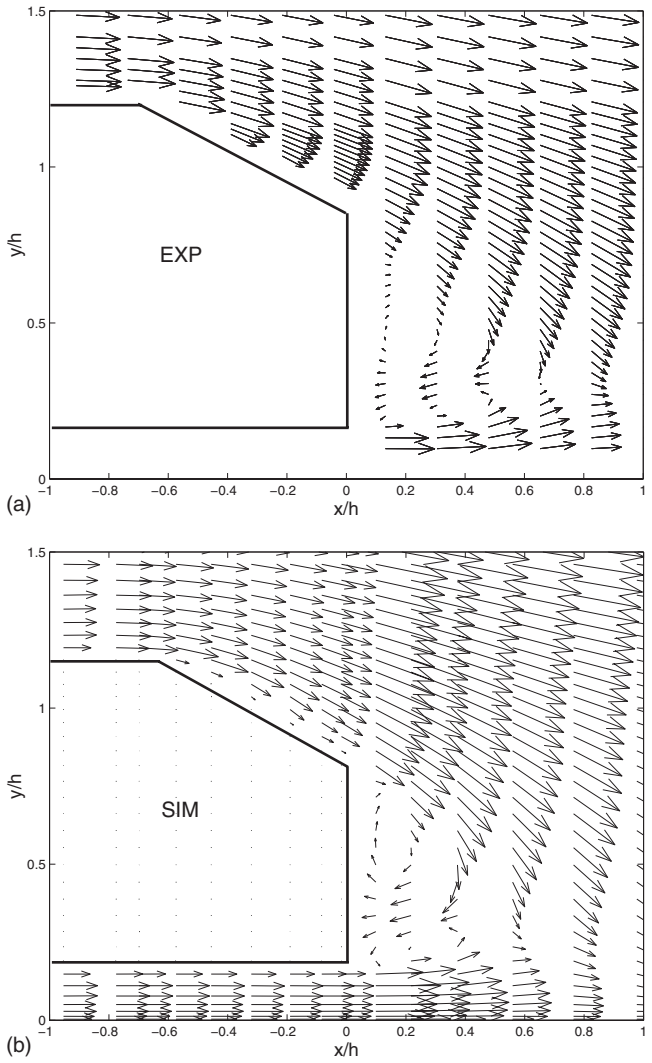

FIG. 10. Mean velocity field in the symmetry plane $z=0$ in the near wake of the Ahmed body, Re=768 000: (a) Experimental measurements of Lienhart *et al.* (Ref. 3) and (b) present LES results.

composed of two contrarotating vortices, whose size and center location compare well with the measurements (see Fig. 10). The length of the recirculation zone is equal to 0.6 in both investigations. The locations of the lower vortex are the same, centered at $(x\approx 0.35, y\approx 0.25)$, whereas they slightly differ for the upper one, with $(x\approx 0.2, y\approx 0.6)$ in the experiments and $(x\approx 0.15, y\approx 0.55)$ for the present LES. Moreover, the minimum of streamwise velocity in the lower vortex core measured in the yz-plane $x=0.278$ [Fig. 11(e)] appears very close to the experimental one, with a difference of about 5%.

B. Mean fields and turbulence statistics on the slant and in the near wake

The mean and turbulent quantities are presented in this section at different streamwise locations over the slant and in the wake of the bluff body. The calculated quantities have been converged over 40 time units. This time interval is much larger than the one used in Ref. 13 and approximately corresponds to the one used for the classical flow around a cylinder in Ref. 38. Some of the results are compared with the velocity measurements of Ref. 3 using a LDA system.

1. Time averaged profiles

As usual, see the review in Ref. 2 all profiles are provided in the symmetry plane $z=0$ (Fig. 12). They globally agree with the LDA measurements both on the slant and within the near wake region.

In the near wake region $(0\leqslant x\leqslant 0.5)$, the LES captures well the magnitude of the mean velocity with a difference less than 7% over the height of the recirculation bubble [Figs. 12(a)–12(c)]. The boundary layer on the ground floor is also well described in the complex flow region where the recirculation bubble interacts with the fluid flowing under the body. The velocity maxima as well as the thickness of the boundary layer agree with the experimental measurements. The turbulent kinetic energy is also well captured [see Fig. 12(e)] especially for the locations and magnitudes of the maxima in the streamwise direction. These maxima correspond to the development of a spanwise-vortex shedding coming from the lower leading edge of the Ahmed body.

The streamwise [Fig. 12(b)] and crossflow [Fig. 12(d)] velocity profiles over the slant show that the turbulent boundary layer thickens from $\delta/h\simeq 7.5\times 10^{-2}$ to $\delta/h\simeq 2.7\times 10^{-1}$. On the upstream part, the agreement between the LES velocity profiles and the LDA measurements is less satisfactory. This discrepancy is related to the differences observed with experiments in the shape of the recirculation bubble, as already discussed in Sec. V A. Indeed, the flow separation observed in LES at the front of the body increases the turbulence production around the symmetry plane and consequently delays the detachment over the slant. Downstream the separation where the flow reattaches, the LES profiles accurately describe the boundary layer, providing both right thickness and velocity maxima. Accordingly, the turbulent kinetic energy within the boundary layer is well described, whereas it is slightly overestimated outside the boundary layer.

The turbulence is mainly produced in the shear region where the recirculation bubble at the flow separation interacts with the boundary layer coming from the roof. More precisely, 30% in simulations and 45% in experiments[3] of the turbulent kinetic energy k in the symmetry plane $z=0$ are produced within the upper half part of the boundary layer along the slant. These productions have been obtained by summing numerically the turbulent kinetic energy within the boundary layer over the slant by using the basic method of rectangles. Moreover, the maximum of k is located in simulations as well as in experiments just downstream of the leading edge of the slant where the flow separates. Nevertheless, for the LES the location is shifted downstream to $x=-0.48$ compared to $x=-0.696$ in the experiments [see Fig. 12(e)] probably as the result of the upstream differences previously discussed (Sec. V A).

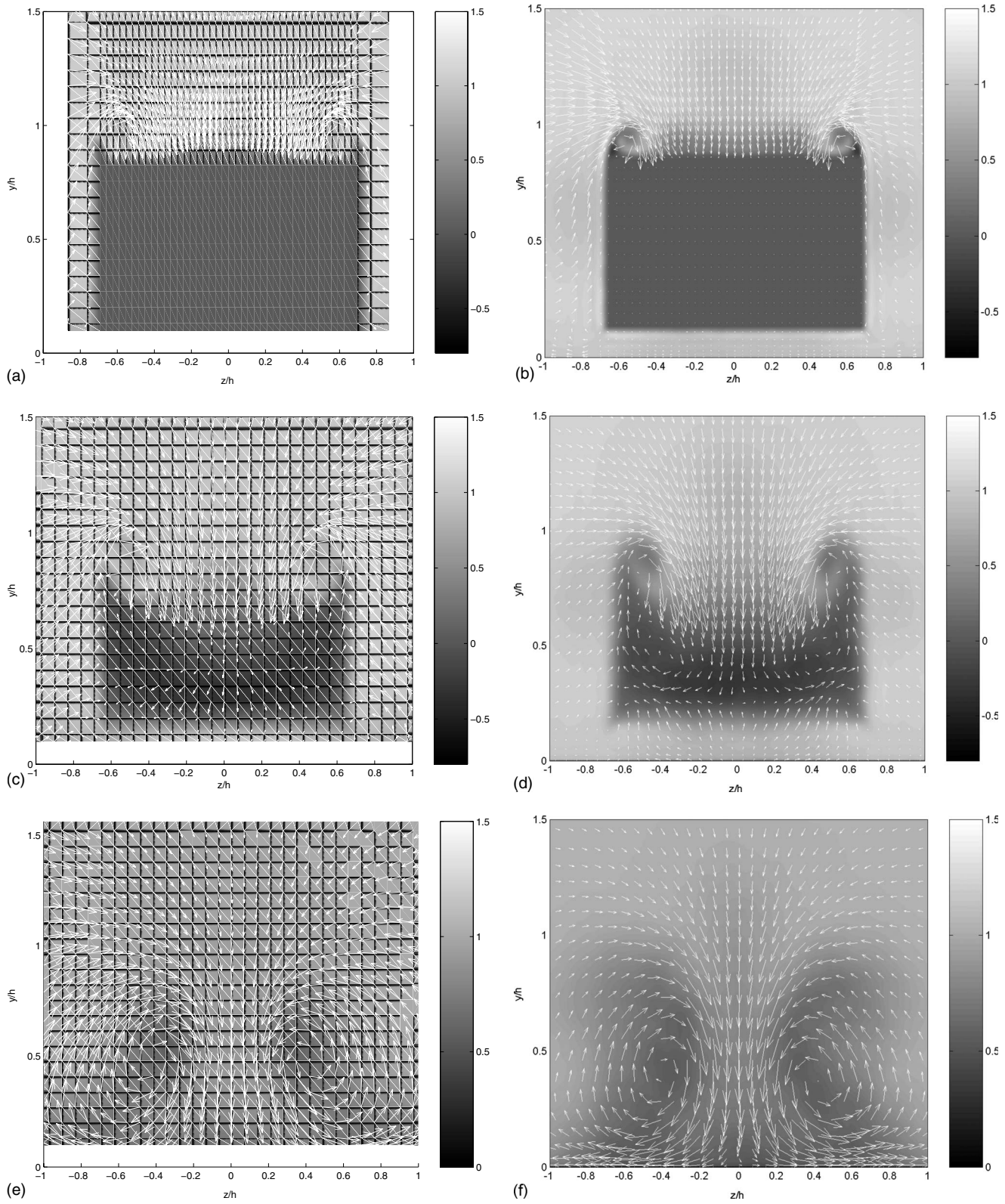

FIG. 11. Mean velocity field and isocounters of the streamwise velocity in the (y,z) planes in the wake of the Ahmed body at Re=768 000: [(a), (c), and (e)] Experimental measurements of Lienhart *et al.* (Ref. 3) and [(b), (d), and (f)] present LES results measured at locations $x/h=-0.132$ [(a) and (b)], $x/h=0.278$ [(c) and (d)], and $x/h=1.74$ [(e) and (f)].

2. Intrinsic spectral turbulence properties in the wake

Turbulence features are here highlighted by using power spectra (see Fig. 13) and also anisotropy invariant maps (Fig. 14). This graphical representation[39] characterizes the state of anisotropy of the wake using preferably the two variables (ξ,η) (see, e.g., Ref. 35) constructed from the second and third invariants of the anisotropy tensor $b_{ij}=\langle u_i' u_j'\rangle/\langle u_k' u_k'\rangle-\delta_{ij}/3$ (δ_{ij} represents the Kronecker symbol and summation over repeated indices is assumed) and defined as $(\xi^3,\eta^2)=(b_{ii}^3/6,b_{ii}^2/6)$.

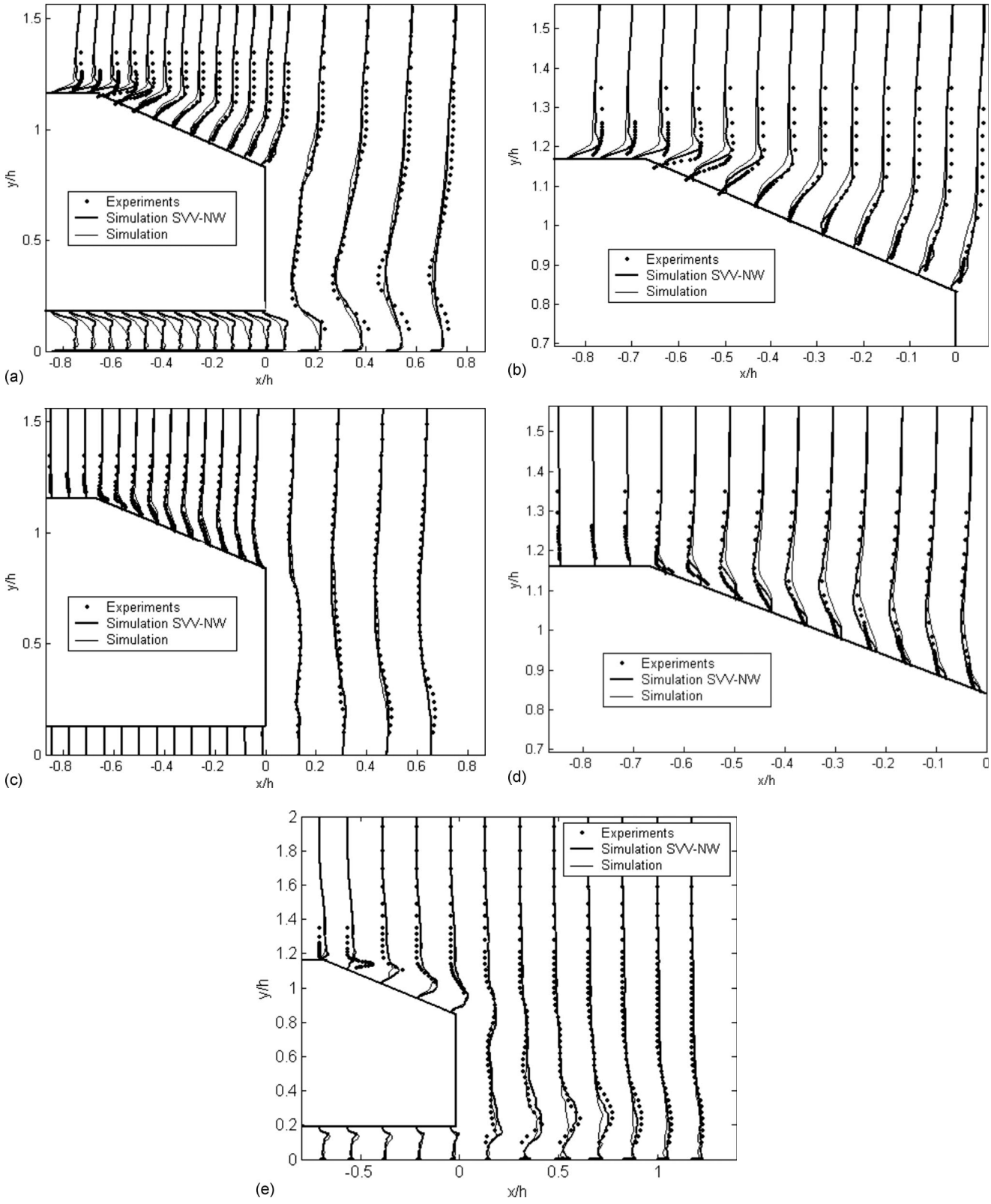

FIG. 12. Turbulence statistics in the symmetry plane $z=0$ over the slant and in the near wake of the Ahmed body at Re=768 000: [(a) and (b)] Profiles of the mean streamwise velocity, [(c) and (d)] profiles of the mean vertical velocity, and (e) profile of the turbulent kinetic energy. Comparisons of the numerical results, with and without near wall treatment, to the experimental results of Lienhart *et al.* (Ref. 3).

The z-spectra of the streamwise velocity fluctuations contain a large range of frequencies, which is consistent with the instantaneous flow visualizations showing small scale structures in the wake [see Fig. 9(d)]. All the spectra show an inertial subrange of width close to one decade from the dimensionless wavenumber, $k_{l_{EI}}$, corresponding to the length scale l_{EI} estimated in Sec. IV C. As known in the case of a fully developed isotropic homogeneous turbulence, the en-

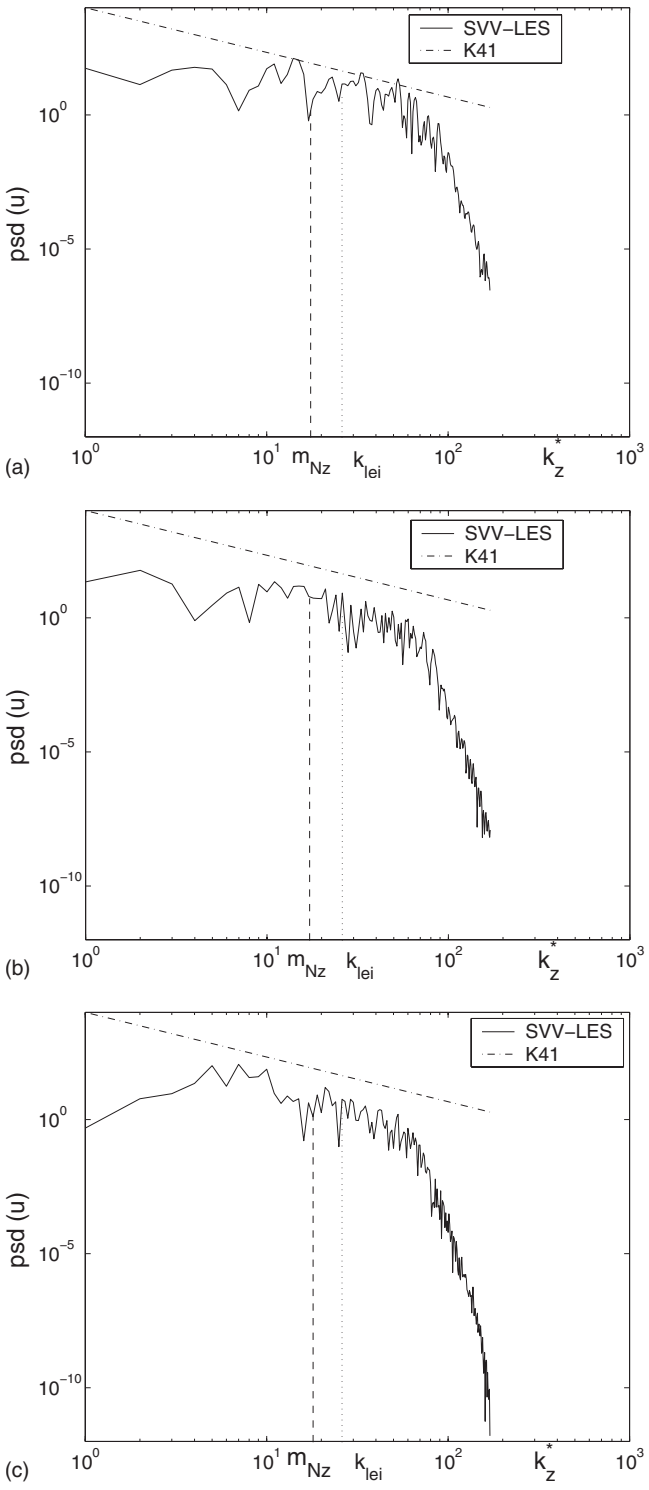

FIG. 13. Power spectral density of the fluctuations of the density u at three locations in the wake. (a) (x=0.27, y=0.44), (b) (x=3.1, y=0.44), and (c) (x=6.83, y=0.44). Comparisons with Kolmogorov theory (K41 curve). The SVV threshold m_N defines the range of frequencies in which the SVV acts.

ergy in this subrange is found to decrease at the Kolmogorov rate $k^{-5/3}$. This is particularly clear in the far wake [Figs. 13(b) and 13(c)]. In the near wake [Fig. 13(a)], the $k^{-5/3}$ behavior appears less clearly due to the fact that the turbulence is less isotropic and homogeneous than farther in the wake.

Figure 14 points out that the LES results respect the realizability diagram of Lumley,[39,35] as the (ξ, η) points remain within the region delimited by the three solid lines. Such diagrams are given at three x-locations in both y- and z-directions. The lack of isotropy in the very near wake is pointed out in Fig. 14(b), 14(d), and 14(f), which correspond to the z-direction. Farther in the wake one observes an accumulation of points at the $(\xi=\eta=0)$ vertex, which indicates an isotropic turbulence. Figures 14(a), 14(c), and 14(e) correspond to the y-direction. Far in the wake and within the boundary layer at the ground $(0 \leqslant y \leqslant 0.1)$, the (ξ, η) values are close to the ones obtained in the classical channel flow [Fig. 14(e)]. Very close to the ground, the turbulence is essentially two components, $\langle v^2 \rangle$ being much smaller than $\langle u^2 \rangle$ and $\langle w^2 \rangle$. The anisotropy (measured by η) reaches a peak at $y^+ \approx 6$. Farther from the ground (up to $y \approx 0.1$), the Reynolds stress is close to being axisymmetric with ξ positive. Outside the ground boundary layer and within the wake $(0.1 \leqslant y \leqslant 1.75)$, the turbulence is axisymmetric with alternatively $(\xi<0, \eta>0)$ and $(\xi>0, \eta>0)$ that is characteristic of the center and of the edges of the mixing layer, respectively. This alternative behavior could be related to the development of several shear layers developing around large structures pointed out in the wake (see Sec. V A).

C. Dissipation rates

In the framework of LES the turbulent kinetic energy is not dissipated at the level of the viscous scales, which are not resolved, but at the SGS level, usually modeled. An advantage of the SVV-LES approach with respect to implicit (ILES) methods, and even on low order standard LES, is that one can easily compute this transfer of energy to the nonresolved scales. With ILES approaches the numerical dissipation is indeed generally not straightforward to determine. When using low order LES, based on first or second order approximation, the problem results from a mixing between the numerical dissipation and the dissipation involved by the SGS model. When high-order methods are concerned, the numerical dissipation becomes negligible, and with the SVV technique the artificial dissipation may be accurately determined. It becomes then possible to provide a relevant computation of the dissipation rate ε of the turbulent kinetic energy.

To establish the expression of ε one has simply to follow the usual methodology (see, e.g., Ref. 35), i.e., in our case to restart from the SVV stabilized Navier–Stokes equations and to deduce the governing equation of the kinetic energy. This partial differential equation is then put in a form that points out the work of the viscous and SGS forces plus a sink term, corresponding to the degradation of kinetic energy in heat. Averaging this sink term and subtracting the part corresponding to the mean flow yields the dissipation rate of the turbulent kinetic energy,

$$\varepsilon = 2\nu(\langle S{:}\widetilde{S}\rangle - \langle S\rangle{:}\langle\widetilde{S}\rangle). \tag{16}$$

In this expression S is the usual strain rate tensor and $\widetilde{S}$ is a similar tensor but computed with the SVV modified differentiation matrices, defined in Eq. (10),

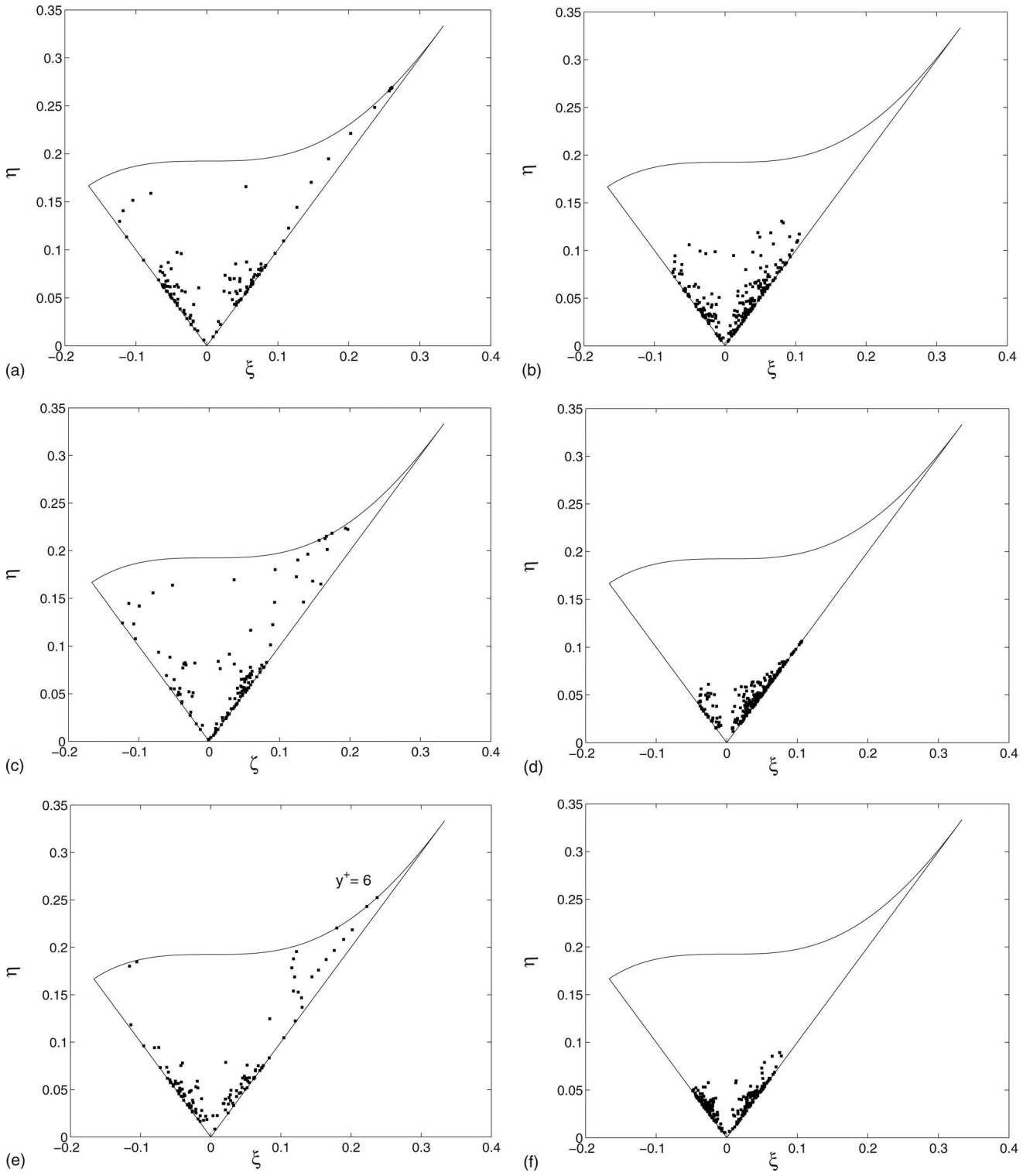

FIG. 14. Sketch of anisotropic tensor b_{ij} in the Lumley triangle (Ref. 35) in the wake of the Ahmed body at Re=768 000: vs the y-axis at left, (a) (x=0.27, z=0), (c) (x=3.1, z=0), and (e) (x=6.83, z=0) and vs the z-axis at right, (b) (x=0.27, y=0.44), (d) (x=3.1, y=0.44), and (f) (x=6.83, y=0.44).

$$S_{ij} = (\partial_i u_j + \partial_j u_i)/2, \quad \widetilde{S}_{ij} = (\widetilde{\partial}_i u_j + \widetilde{\partial}_j u_i)/2. \tag{17}$$

All details and justification for expression (16) of the dissipation rate may be found in Ref. 40.

Profiles of the dissipation rate have been computed in the near wake versus the y-vertical and z-spanwise directions and at different abscissa, as shown in Fig. 15. On the contrary to the other turbulence statistics, computed over 40 time units, for technical reasons the dissipation rates have only been computed over 20 time units. Moreover, computations of derivatives of the velocity components are involved. Consequently, the dissipation rate profiles are not yet completely converged. However the trends can be clearly discerned: The amplitudes of the profiles are decreasing with respect to x, i.e., the distance to the car model, and these profiles are coherent with the topology of the flow, showing

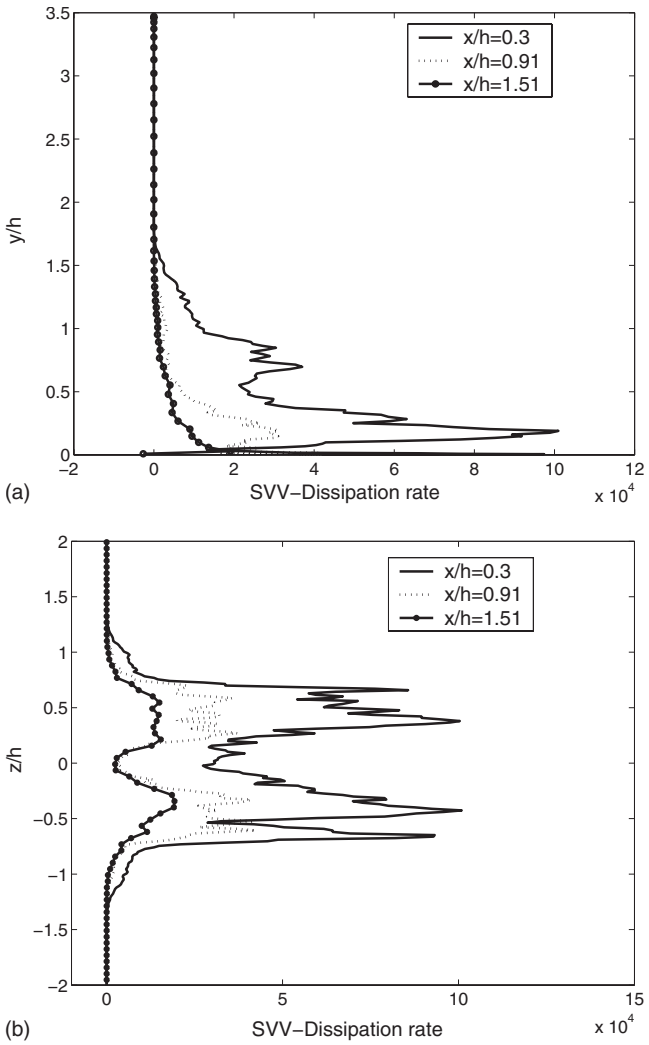

FIG. 15. Dissipation rate of the turbulent kinetic energy times Re at three different abscissa in the wake: (a) vs the vertical direction, $z=0$; (b) vs the spanwise direction, $y=0.674$.

maxima in the trailing vortices that develop downstream. Note that similar results can be obtained at the location of the car model, showing maxima in the near wall region. Moreover, we have also compared the viscous dissipation, using the usual expression of ε by substituting $\tilde{S}_{ij}$ with S_{ij} in Eq. (16), to the results presently discussed. As could be expected, due to the very large value of the Reynolds number, the contribution of the viscous dissipation is about three orders of magnitude smaller than the global dissipation, essentially provided by the SVV stabilization term.

D. Comparisons of simulation with or without near wall treatment

The efficiency of the near wall treatment, SVV-NW (Sec. III D), is assessed by comparing results of simulations performed with and without relaxation of the SVV stabilization in the NW region. The profiles of mean velocity and turbulence quantities obtained without NW treatment have been included in Fig. 12. As expected, the SVV-NW results predict a more turbulent boundary layer along the slant with values of the turbulent kinetic energy k in better agreement with the LDA measurements of Ref. 3 [see Fig. 12(e)]. Indeed, one observes an increase by about 25% of the production of k, production which is also more concentrated on the upper part of the slant boundary layer, in agreement with experimental observations. The agreement with the experimental location of the maximum of k, $x=-0.696$, is also much better, $x=-0.48$, rather than $x=-0.39$. Currently, the upper half part of the slant provides 30% of the turbulence produced over the slant in the SVV-NW simulations (Sec. V B) to be compared to 45% for the experiments[3] and to 20% only without NW treatment. This increase of turbulence production is associated with the development of horseshoe vortices along the slant [Fig. 9(a)], which are not observed without NW treatment and which consequently induce a stronger unsteadiness. The thickness of the boundary layer on the roof appears thinner with SVV-NW, $\delta \simeq 7.5 \times 10^{-2}$, rather than $\delta \simeq 8.5 \times 10^{-2}$. This behavior is clearly preserved over the slant, thus providing a better agreement with the LDA measurements.[3] Moreover, SVV-NW tends to diminish the underestimation of the streamwise velocity far above the slant with respect to the measurements. The NW treatment also acts in the near wake of the bluff body, where the magnitude of the turbulent kinetic energy provided by the lower spanwise-vortex shedding agrees better with the experiments [see Fig. 12(e)].

VI. CONCLUDING REMARKS

A high-order LES based on a SVV stabilization technique has been applied satisfactorily for the first time to the industrial turbulent flow over the Ahmed body. An original near wall treatment based on a local relaxation of the SVV threshold has been implemented, which has considerably improved the results, particularly the production of turbulence over the slant.

Valuable results have been obtained in globally good agreement with the reference experimental results of Ref. 3. The topology of the flow has been recovered as the partial separation of the turbulent boundary layer at the edge of the slant controlled by two strong contrarotative trailing vortices. Horseshoelike vortices over the slant have also been captured by the SVV-LES results. Mean velocity as well as turbulence kinetic energy profiles fairly agree with experimental measurements in the symmetry plane $z=0$. More intrinsic properties of the turbulence were pointed out as the $k^{-5/3}$ energy density decay in the inertial range as well as the anisotropy properties.

However, improvements of the results should come from a better description of the turbulent boundary layer dynamics over the roof since the separation of the flow at the body front is expected to be the main cause of the discrepancies with experiments. It should also be mentioned as a consequence that the drag coefficient that we presently obtain is overestimated. Solutions as the decrease of the adverse pressure gradient by the confinement as well as the implementation of viscosity kernel parameters that could be selected adaptively by relating them to the dynamics of the flow, i.e., the strain field, would involve higher resolutions with pro-

hibitive computational costs. A key issue would come certainly from the development of a relevant NW model, in conjunction with the use of our penalty-type technique in order to take into account the right level of turbulence kinetic energy production.

ACKNOWLEDGMENTS

The calculations were carried out on the NEC SX8 vector computer of the CNRS computational center IDRIS (Project No. 074055). Computational resources of the mesocentre SIGAMM of the OCA were also used. The authors gratefully acknowledge support from the CNRS through the DFG-CNRS program "LES of complex flows." J. Fröhlich, B. E. Launder, R. J. A. Howard, and B. Viaud are gratefully acknowledged for their comments and advices on the results interpretation.

[1] S. R. Ahmed and G. Ramm, "Salient features of the time-averaged ground vehicle wake," SAE Paper No. 840300, 1984.
[2] R. Manceau and J.-P. Bonnet, 10th ERCOFTAC (SIG-15)/IAHR/QNET-FD Workshop on Refined Turbulence Modelling, Université de Poitiers, France, 10–11 October 2002, edited by R. Manceau and J.-P. Bonnet.
[3] H. Lienhart, C. Stoots, and S. Becker, DGLR Fach Symposium der AG STAB, Stuttgart University, 15–17 November 2000.
[4] A. Spohn and P. Gillieron, *Proceedings of IUTAM Symposium on Unsteady Separated Flows, Toulouse, 2002* (EDP Sciences, 2002).
[5] P. Gillieron and F. Chometon, "Modelling of stationary three-dimensional detached airflows around an Ahmed reference body," Third International Workshop on Vortex, ESAIM Proceedings **7**, 173 (1999).
[6] L. Durand, M. Kuntz, and F. Menter, "Validation of CFX-5 for the Ahmed car body," CFX Validation Report No. CFX-Val 13/1002, 2002.
[7] T. Han, "Computational analysis of three-dimensional turbulent flow around a bluff body in ground proximity," AIAA J. **27**, 1213 (1989).
[8] T. J. Craft, S. E. Gant, H. Iacovides, B. E. Launder, and C. M. E. Robinson, "Computational study of flow around the Ahmed car body (case 9.4)," *Proceedings of the Ninth ERCOFTAC/IAHR Workshop on Refined Turbulence on Modelling*, Darmstadt University of Technology, Germany, 4–5 October 2001, edited by B. Basara (AVL GmbH, Graz, 2001).
[9] F. R. Menter and M. Kuntz, "Development and application of a zonal DES turbulence model for CFX-5," CFX internal report, 2003.
[10] E. Guilmineau, "Computational study of flow around a simplified car body," J. Wind. Eng. Ind. Aerodyn. **96**, 1207 (2007).
[11] S. Krajnovic and L. Davidson, "Flow around a simplified car," J. Fluids Eng. **127**, 907 (2005); **127**, 919 (2005).
[12] R. J. A. Howard and M. Pourquie, "Large eddy simulation of an Ahmed reference model," J. Turbul. **3**, 1 (2002).
[13] M. Hinterberger, M. Garcia-Villalba, and W. Rodi, in *Lecture Notes in Applied and Computational Mechanics/The Aerodynamics of Heavy Vehicles: Trucks, Buses, and Trains*, edited by R. McCallen, F. Browand, and J. Ross (Springer, New York, 2004).
[14] E. Fares, "Unsteady flow simulation of the Ahmed reference body using a lattice Boltzmann approach," Comput. Fluids **35**, 940 (2006).
[15] V. Borue and S. Orszag, "Local energy flux and subgrid-scale statistics in three-dimensional turbulence," J. Fluid Mech. **366**, 1 (1998).
[16] C. Fureby and F. F. Grinstein, "Monotonically integrated large eddy simulation of free shear flow," AIAA J. **37**, 19 (1999).
[17] F. F. Grinstein and C. Fureby, *ECCOMAS CFD 2006, Delft, The Netherland 2006*, edited by P. Wesseling, J. Onate, and J. Périaux (TU Delft, Delft, 2006).
[18] T. J. R. Hugues, L. Mazzei, and A. A. Oberai, "The multiscale formulation of large eddy simulation: Decay of homogeneous isotropic turbulence," Phys. Fluids **13**, 505 (2001).
[19] J. L. Guermond, J. T. Oden, and S. Prudhomme, "Mathematical perspectives on large eddy simulation models for turbulent flows," J. Math Fluid Mech. **6**, 194 (2004).
[20] E. Tadmor, "Convergence of spectral methods for non linear conservation laws," SIAM (Soc. Ind. Appl. Math.) J. Numer. Anal. **26**, 30 (1989).
[21] G. S. Karamanos and G. E. Karniadakis, "A spectral vanishing viscosity method for large-eddy simulation," J. Comput. Phys. **163**, 22 (2000).
[22] R. M. Kirby and G. E. Karniadakis, "Coarse resolution turbulence simulations with spectral vanishing viscosity-large eddy simulation (SVV-LES)," J. Fluids Eng. **124**, 886 (2002).
[23] R. M. Kirby and S. J. Sherwin, "Stabilization of spectral/hp element methods through spectral vanishing viscosity: Application to fluid mechanics modelling," Comput. Methods Appl. Mech. Eng. **195**, 3128 (2006).
[24] R. Pasquetti, "Spectral vanishing viscosity method for large-eddy simulation of turbulent flows," J. Sci. Comput. **27**, 365 (2006).
[25] E. Severac and E. Serre, "A spectral viscosity LES for the simulation of turbulent flows within rotating cavities," J. Comput. Phys. **226**, 1234 (2007).
[26] C. Sabbah and R. Pasquetti, "A divergence-free multidomain spectral solver of the Navier–Stokes equations in geometries of high aspect ratio," J. Comput. Phys. **139**, 359 (1998).
[27] L. Cousin and R. Pasquetti, *Advances in Scientific Computing and Applications*, edited by Y. Lu, W. Sun, and T. Tang (Science, Beijing, 2004), pp. 133–143.
[28] Y. Maday, S. M. O. Kaber, and E. Tadmor, "Legendre pseudo-spectral viscosity method for nonlinear conservation laws," SIAM (Soc. Ind. Appl. Math.) J. Numer. Anal. **30**, 321 (1993).
[29] J. Kim, D. Kim, and H. Choi, "An immersed-boundary finite volume method for simulations of flow in complex geometries," J. Comput. Phys. **171**, 132 (2001).
[30] J. Yang and E. Balaras, "An embedded-boundary formulation for large-eddy simulation of turbulent flows interacting with moving boundaries," J. Comput. Phys. **215**, 12 (2006).
[31] P. Angot, C. H. Bruneau, and P. Fabrie, "A penalization method to take into account obstacles in incompressible viscous flows," Numer. Math. **81**, 497 (1998).
[32] R. Pasquetti, R. Bwemba, and L. Cousin, "A pseudo-penalization method for high Reynolds number unsteady flows," Appl. Numer. Math. **58**, 946 (2008).
[33] U. Piomelli and E. Balaras, "Wall-layer models for large-eddy simulations," Annu. Rev. Fluid Mech. **34**, 349 (2002).
[34] R. Pasquetti, "Spectral vanishing viscosity method for LES: Sensitivity to the SVV control parameters," J. Turbul. **6**, N12 (2005).
[35] S. B. Pope, *Turbulent Flows* (Cambridge University Press, Cambridge, 2000).
[36] H. Tennekes and J. Lumley, *A First Course in Turbulence* (MIT, Cambridge, MA, 1972).
[37] G. Franck, N. M. Nigro, M. A. Storti, and J. D'Elia, in *Mechanica Computacional*, edited by M. B. Rosales, V. H. Cortinez, and D. V. Bambill (Bahia Blanca, 2003), Vol. XXII.
[38] A. Kravchenko and P. Moin, "Numerical studies of flow over a circular cylinder at Re=3900," Phys. Fluids **12**, 403 (2000).
[39] J. L. Lumley, "Computational modeling of turbulent flows," Adv. Appl. Mech. **18**, 123 (1978).
[40] R. Pasquetti, *ECCOMAS CFD 2006, Delft, The Netherlands, 2006*, edited by P. Wesseling, J. Onate, and J. Périaux (TU Delft, Delft, 2006).